






Titanium-containing high entropy oxide (Ti-HEO): A redox expediting electrocatalyst towards lithium polysulfides for high performance Li-S batteries

Hassan Raza^{1,2,§}, Junye Cheng^{1,§} , Jingwei Wang¹, Subash Kandasamy³, Guangping Zheng² , and Guohua Chen³ 

¹ Department of Materials Science, Shenzhen MSU-BIT University, Shenzhen 517182, China

² Department of Mechanical Engineering, Research Institute for Smart Energy, The Hong Kong Polytechnic University, Hung Hom, Kowloon, Hong Kong SAR, China

³ School of Energy and Environment, City University of Hong Kong, Tat Chee Avenue, Kowloon, Hong Kong SAR, China

[§] Hassan Raza and Junye Cheng contributed equally to this work.

Received: 1 November 2023 / Revised: 25 January 2024 / Accepted: 1 February 2024

ABSTRACT

Since lithium sulfur (Li-S) energy storage devices are anticipated to power portable gadgets and electric vehicles owing to their high energy density (2600 Wh·kg⁻¹); nevertheless, their usefulness is constrained by sluggish sulfur reaction kinetics and soluble lithium polysulfide (LPS) shuttling effects. High electrically conductive bifunctional electrocatalysts are urgently needed for Li-S batteries, and high-entropy oxide (HEO) is one of the most promising electrocatalysts. In this work, we synthesize titanium-containing high entropy oxide (Ti-HEO) (TiFeNiCoMg)O with enhanced electrical conductivity through calcining metal-organic frameworks (MOF) templates at modest temperatures. The resulting single-phase Ti-HEO with high conductivity could facilitate chemical immobilization and rapid bidirectional conversion of LPS. As a result, the Ti-HEO/S/KB cathode (with 70 wt.% of sulfur) achieves an initial discharge capacity as high as ~1375 mAh·g⁻¹ at 0.1 C, and a low-capacity fade rate of 0.056% per cycle over 1000 cycles at 0.5 C. With increased sulfur loading (~5.0 mg·cm⁻²), the typical Li-S cell delivered a high initial discharge capacity of ~607 mAh·g⁻¹ at 0.2 C and showcased good cycling stability. This work provides better insight into the synthesis of catalytic Ti-containing HEOs with enhanced electrical conductivity, which are effective in simultaneously enhancing the LPS-conversion kinetics and reducing the LPS shuttling effect.

KEYWORDS

titanium containing high entropy oxide (Ti-HEOs), multi-metal-MOFs template method, electrical conductivity, lithium-sulfur batteries, catalytic conversion

1 Introduction

Recent developments in rechargeable lithium-sulfur batteries (LSBs) seek to provide alternative energy storage devices with a high energy density of 2600 Wh·kg⁻¹ [1, 2]. The attractive characteristics of elemental sulfur, including high theoretical capacity (~1675 mAh·g⁻¹), natural abundance, affordability, and environmental compatibility, have made it a desirable storage system [3–9]. However, the high intrinsic resistivity of sulfur (1024 Ω·cm) and its discharged counterpart Li₂S/Li₂S₂ (>1014 Ω·cm), the existence of lithium polysulfides (LPS) that shuttle between electrodes, slow redox kinetics, and structural instability of the sulfur cathode during cycling all lead to irreversible sulfur loss, fast capacity fading, and low Coulombic efficiency [10, 11]. Considerable endeavors have been dedicated towards enhancing

the electrochemical efficacy of LSBs by incorporating resilient hosts, including polar and non-polar substances such as carbonaceous materials, metal sulfides, nitrides, and oxides, into the sulfur cathode [12–24]. Nevertheless, the LPS can be partially encapsulated through the use of these passive methods. Dredging efficiently has recently been shown to be more effective than blocking LPS entirely in the cathode vicinity [25]. Therefore, it is imperative to investigate a highly efficient electrocatalyst that exhibits enhanced electrical and ionic conductivities in order to mitigate the phenomenon of LPS shuttling, while simultaneously accelerating the transformation of soluble LPS into insoluble products (i.e., Li₂S/Li₂S₂) [26–31].

Owing to the revolutionary concept of configurational entropy driven phase stability, high entropy oxide (HEO) has attracted growing attention as a crystalline multicomponent material with

© The Author(s) 2024. Published by Tsinghua University Press. The articles published in this open access journal are distributed under the terms of the Creative Commons Attribution 4.0 International License (<http://creativecommons.org/licenses/by/4.0/>), which permits use, distribution and reproduction in any medium, provided the original work is properly cited.

Address correspondence to Junye Cheng, chengjunye@smbu.edu.cn; Guangping Zheng, mmzheng@polyu.edu.hk; Guohua Chen, ghchen1963@gmail.com

unique and stable phases [32–34]. The synthetically generated HEOs are being employed as both positive and negative electrode materials, as well as solid-state electrolytes, in energy dense lithium-ion battery technologies [35, 36]. Given to potential importance of metal cation centers in metal oxides for the rapid catalytic conversion of LPS [37], multicomponent metal oxides (i.e., $\text{Mg}_{0.6}\text{Ni}_{0.4}\text{O}$, $\text{Mg}_{0.8}\text{Cu}_{0.2}\text{O}$, NiFe_2O_4 , NiCo_2O_4) have been extensively investigated to act as an effective modulator of LPS, maximizing the synergistic effects of multiple metal cations [38, 39]. Nevertheless, the inherent insulating properties of these metal oxides pose a notable drawback, rendering them impractical for use as a modulator of LPS in LSBs.

Previously, titanium (Ti) was successfully incorporated into multi-metal oxides ($\text{Ti}_x\text{FeCoNi}_y\text{O}$) to enhance the electrical conductivity, and fabricated material showcased low electrical resistivity of $35 \pm 3 \mu\Omega\cdot\text{cm}$ equivalent to that of RuO_2 single crystal and considerably lower than that of indium tin oxide (ITO) [40, 41]. $\text{TiFeCoNiCu}_x\text{O}$, Ti-containing HEO (Ti-HEO), likewise showed poor electrical resistivities [40]. The improved electrical conductivity of Ti-HEOs has been attributed to the existence of oxygen defects generated by the incorporation of Ti atoms. The Ti-HEOs exhibit a notable level of electrical conductivity and possess a substantial number of exposed active sites containing numerous cations [42]. Therefore, the Ti-HEOs are anticipated to effectively anchor LPS, decrease the shuttling effect, and boost LSB performance.

Herein, titanium-containing high entropy oxides (Ti-HEO) with enhanced electrical conductivity are fabricated by same facile synthesis technique of low-temperature calcination of metal organic framework (MOF) templates which has been successfully applied for the formulation of HEO ($\text{Ni}_{0.2}\text{Co}_{0.2}\text{Cu}_{0.2}\text{Mg}_{0.2}\text{Zn}_{0.2}\text{O}$ (HEO850) in our previous work [42, 43]. The Ti-HEO/S/KB cathode outperforms HEO850/S/KB [42] particularly at high sulfur loadings due to its superior catalytic conversion properties over LPS and increased electrical conductivities. Typically, at a sulfur loading of $\sim 3.4 \text{ mg}\cdot\text{cm}^{-2}$, it exhibits a high initial discharge capacity of $\sim 1246 \text{ mAh}\cdot\text{g}^{-1}$ and it is retained at $\sim 542 \text{ mAh}\cdot\text{g}^{-1}$ with a small capacity decay rate of 0.056% per cycle over 1000 cycles at 0.5 C.

2 Experimental section

Details of the experimental section are provided in the Electronic Supplementary Material (ESM).

3 Results and discussion

3.1 Microstructural characteristics of Ti-HEO

Figure S1 in the ESM presents a schematic illustrating the fabrication process of Ti-HEO samples through the calcination of multi-metal MOFs (M-MOFs) at various temperatures, specifically 450 °C, 650 °C, and 850 °C [44, 45]. Multiple impurity phases were detected in the samples generated at 450 and 650 °C. However, a single-phase was succeeded by subjecting the M-MOFs templates to a heating process at 850 °C for a duration of 10 hours, as identified using X-ray diffraction (XRD) patterns depicted in Fig. 1(a). XRD peaks could be indexed to (111), (200), (220), (310), and (222) lattice planes consistent with those of rocksalt structure [46]. The formation of Ti-HEO at higher temperature (1000 °C) is further investigated. As expected, the single-phase Ti-HEO (obtained at 850 °C) did not show any

variation in XRD pattern (Fig. S2 in the ESM). This compelling evidence solidifies the notion that 850 °C represents the optimal temperature for the synthesis of a single-phase Ti-HEO. The XRD patterns of solid solutions with less than 5 constituent metal elements (whose compositions are listed in Table S1 in the ESM) are shown in Fig. 1(b), suggesting that there are multiple phases in the solid solutions even when the calcination temperature is as high as 1000 °C. Results implies that both higher calcination temperatures and maximum configurational entropy (S_{config}) are needed to produce a single-phase crystal structure in Ti-HEOs. For this reason, entropy-dependent single-phase production in HEOs requires at least ≥ 5 metal component elements [32, 42].

The Raman spectra of bare Ti-HEO and Ti-HEO/KB exhibits observable Raman shifts at 163, 333, and 712 cm^{-1} indicating that Ti-HEO exists in the composite material. The determination of intensity ratio (I_D/I_G) between the D- and G-bands provides valuable insights about the level of graphitization demonstrated by carbon-based materials. The value of I_D/I_G (1.05) for Ti-HEO/KB composite is slightly higher than that of bare KB ($I_D/I_G = 1.01$), advocating that Ti-HEO/KB possesses more lattice defective sites (Fig. 1(c)). These defects could be beneficial for anchoring LPS, as depicted in detail in the section that follows. The SEM images of Ti-HEO (Fig. 1(d) and Figs. S3(a) and S3(b) in the ESM) depict the expected irregular morphology, the average particle size is 1 μm (Inset: Fig. 1(d)). The transmission electron microscope (TEM) image further validates the morphology and size ($\sim 562 \text{ nm}$) of the Ti-HEO which has high crystallinity (Fig. 1(e) and Fig. S3(c) in the ESM). High-resolution TEM (HRTEM) showcases the typical lattice fringes, elucidating a rocksalt crystal structure and a d-spacing (0.24 nm) in consistent with that of the (111) lattice plane (Inset; Fig. 1(e) and Fig. S3(d) in the ESM). It is obvious from the selected area diffraction (SAED) patterns that Ti-HEO has a polycrystalline structure, and the diffraction rings (Fig. 1(f)) could be indexed to a rocksalt structure, which agrees with XRD results. Likewise, EDX analysis demonstrates the homogeneous spatial distribution and equimolar atomic ratio of metal cations throughout the Ti-HEO sample (Fig. 1(g) and Fig. S3(e) in the ESM).

The surface characteristics and oxidation states of Ti-HEO are additionally ascertained using X-ray photoelectron spectroscopy (XPS). The incorporated five metal elements (i.e., Ni, Mg, Ti, Fe, Co) and oxygen exist in the survey spectrum (Fig. S4 in the ESM) and binding energies of all elements are listed (Table S2 in the ESM). The deconvolution of Ni 2p peak indicates the presence of $\text{Ni}^{2+} 2p_{3/2}$ and $\text{Ni}^{2+} 2p_{1/2}$ species corresponding to binding energies of ~ 855.6 and 873.1 eV , respectively, which are accompanied by typical satellite peaks [47]. The peaks correspond to Co 2p could be fitted into $\text{Co}^{2+} 2p_{3/2}$ located at $\sim 780.9 \text{ eV}$ and $\text{Co}^{2+} 2p_{1/2}$ at $\sim 796.5 \text{ eV}$ with satellite features, suggesting the oxidation state of Co is with 2^+ valence [48] (Figs. S5(a) and S5(b) in the ESM). In the fine scan of Fe 2p (Fig. S5(c) in the ESM), the characteristics of spin-orbit coupling are witnessed with two strong photoemission peaks around at ~ 710.6 and 725.0 eV corresponding to $\text{Fe}^{2+} 2p_{3/2}$ and $\text{Fe}^{2+} 2p_{1/2}$, respectively, along with their satellite shoulder peaks. The fitted peak at around $\sim 713.7 \text{ eV}$ could be associated with $\text{Fe}^{3+} 2p_{3/2}$ [49]. The results indicate Fe^{2+} , Fe^{3+} species could exist in the Ti-HEO samples. Figure S5(d) in the ESM represents the Mg 1s high resolution spectra, suggesting Mg element is with the 2^+ valence state [47]. The Ti 2p spectra can be deconvoluted by considering the contributions of Ti^{4+} , Ti^{3+} , Ti with strong photoemission peaks (Fig. S5(e) in the ESM). Three oxygen species including lattice oxygen (O^{2-}), absorbed oxygen (O_2^{2-}) and

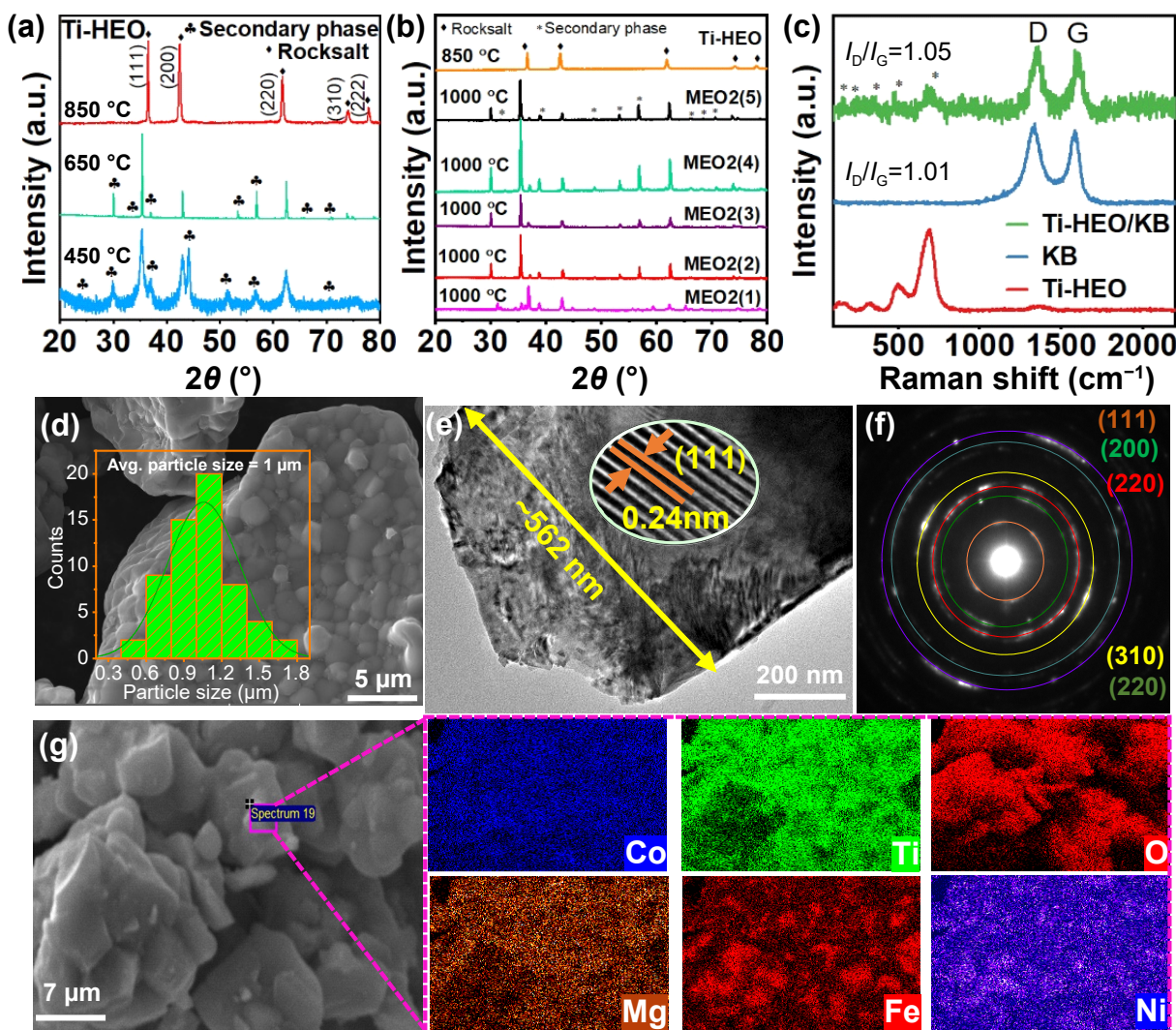


Figure 1 (a) The XRD patterns of Ti-HEO at different calcination temperatures. (b) De-stabilized solid solution with the removal of any metal component from the composition of Ti-HEO. (c) Raman spectroscopy of Ti-HEO, KB and Ti-HEO/KB composite. (d) SEM image (inset: particle size distribution) of Ti-HEO samples. (e) TEM image (inset: HETRM). (f) SAED patterns. (g) EDX elemental mapping of incorporated elements.

hydroxyl species (OH^-) are also identified with the XPS signals at ~ 529.3 , ~ 530.3 , and ~ 531.5 eV, respectively (Fig. S5(f) in the ESM), which are believed to be favorable for the interaction between Li^+ in the LPS and oxygen, ultimately facilitating the enhanced electrochemical performance of Ti-HEOs.

After the incorporation of sulfur in the Ti-HEO/S/KB composite, its morphology is further characterized by SEM. Figures S6(a) and S6(b) in the ESM showcase the existence of orthorhombic sulfur with well-retained morphology of Ti-HEO could be observed in the composite sample. The uniform sulfur distribution can also be validated with EDX elemental mapping (Fig. S6(c) in the ESM).

3.2 Evaluation on the electrocatalytic performance

The catalytic characteristics of Ti-HEO on the transformation of LPS into insoluble $\text{Li}_2\text{S}/\text{Li}_2\text{S}_2$ are evaluated in symmetric batteries (Fig. 2(a)) with corresponding electrodes of Ti-HEO/KB in 0.25 M Li_2S_6 electrolyte solution. Cyclic voltammetry (CV) curves scanned at $10 \text{ mV}\cdot\text{s}^{-1}$ in voltage window from -1 to 1 V (Fig. 2(b)) represent the Ti-HEO/KB cathodes have discrete peaks at ~ 0.04 , 0.74 , 0.10 , -0.04 , -0.10 , and -0.74 V , resulting from oxidation and reduction of sulfur species. In the first cycle (first scan to $+1 \text{ V}$)

with a cell open-circuit voltage (0 V), it is reasonable to speculate that the peak a (at $\sim 0.04 \text{ V}$) could be ascribed to continuous oxidation of LPS to elemental sulfur ($\text{Li}_2\text{S}_6 \rightarrow \text{S}_8$) at the working electrode, which is coupled with the reduction reaction ($\text{S}_8 \rightarrow \text{Li}_2\text{S}_6$) at the counter electrode [50]. Similarly, peak b ($\sim 0.74 \text{ V}$) is due to the oxidation of Li_2S_6 to sulfur, which is integrated with reduction of Li_2S_6 to Li_2S_2 or Li_2S at working or counter electrodes, respectively. Peak c ($\sim 0.10 \text{ V}$) is attributed to the reformation of soluble LPS (Li_2S_6) by electrochemical sulfur reduction at working electrode and oxidation of $\text{Li}_2\text{S}_2/\text{Li}_2\text{S}$ at counter electrode. Additional evidence for the switching of response between working and counter electrodes is provided by the reversal in polarity of peaks d (at -0.04 V), peak e (-0.74 V), and peak f (-0.10 V) [51, 52]. The overlapping curves for the first four cycles of symmetric batteries elucidate the enhanced electrochemical reversibility of Ti-HEO containing cathode. Furthermore, without Li_2S_6 , the symmetric cells display almost negligible capacitive current, indicating Li_2S_6 as the only electrochemically active species in the reaction. In contrast to KB, the Ti-HEO/KB cathodes with higher current response and narrower peak separation indicate the accelerated kinetics of LPS conversion (Fig. 2(c)). The chronoamperometry (CA) curves (Fig. 2(d)) manifest a

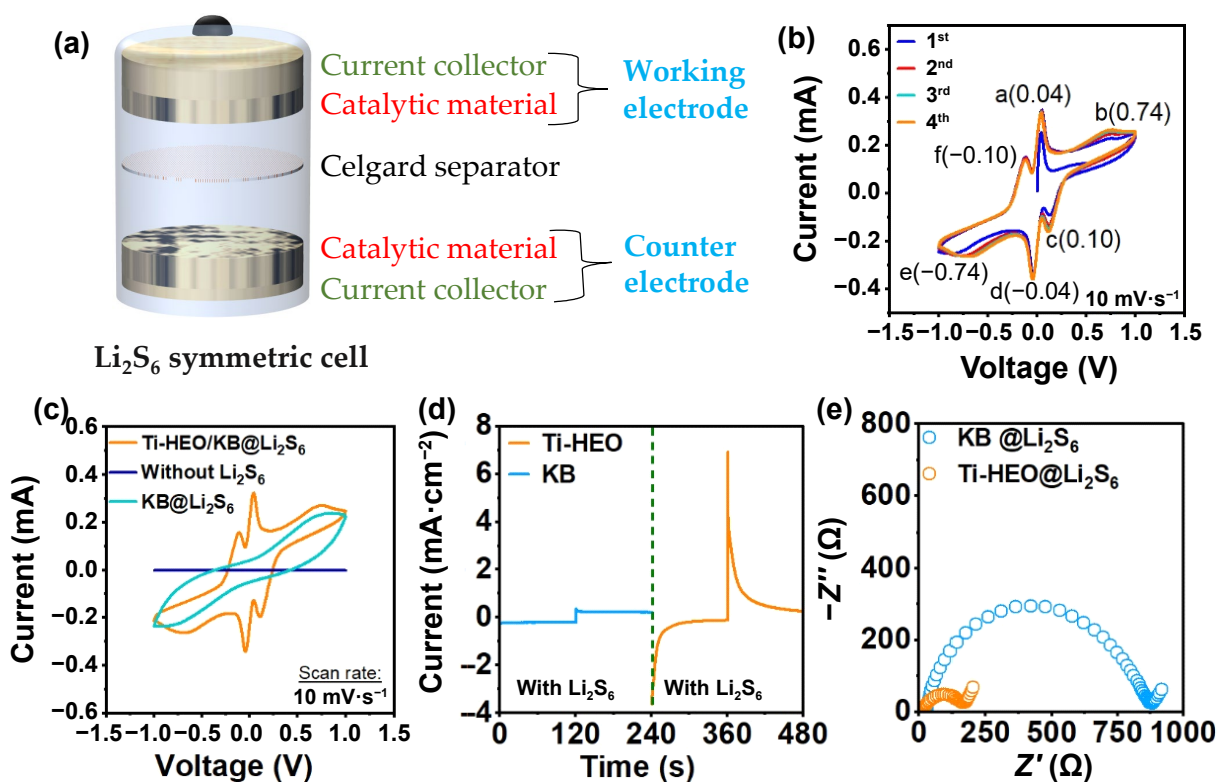


Figure 2 (a) Schematic of Li_2S_6 symmetric cell. (b) CV curves of Ti-HEO for 4 cycles at $10 \text{ mV}\cdot\text{s}^{-1}$. (c) Comparison of CV for Ti-HEO/KB, bare KB symmetric cells with and without Li_2S_6 . (d) Chronoamperometry curves of bare KB and Ti-HEO with Li_2S_6 electrolyte. (e) Comparison of EIS for Ti-HEO@ Li_2S_6 and bare KB@ Li_2S_6 symmetric cells.

superior lithiation/de-lithiation current density of Ti-HEO/KB as compared to those of bare KB, further confirming the favorable effect of Ti-HEO on accelerating the redox kinetics. Figure 2(e) highlights that Ti-HEO/KB has a smaller semicircle, signifying a lower charge transfer resistance ($R_{ct} \approx 160 \Omega$) in comparison to bare KB ($R_{ct} \approx 875 \Omega$). This observation suggests the presence of enhanced electron routes facilitated by incorporated titanium containing HEOs.

The improved redox kinetics is frequently examined in conjunction with the facilitated diffusion of Li -ions. Accordingly, CV measurements are conducted in typical LSBs under various scan speed from 0.1 to $0.5 \text{ mV}\cdot\text{s}^{-1}$, with Ti-HEO/S/KB or S/KB cathode and lithium metal anode (Figs. 3(a) and 3(b)). Both cathodes display distinct reduction and oxidation peaks. Since Li^+ diffusion is restricted during the diffusion-controlled reaction at the sulfur cathode, the CV curve is highly polarized at fast scan rates. The demoted polarization could be evident in Ti-HEO/S/KB cells (Fig. 3(a)) since the shifts in peak positions for the cells are lesser than those for the S/KB cells. Additionally, the Li^+ ion diffusion rate could be calculated using the Randles-Sevcik equation: $I_p = (2.69 \times 10^5) n^{1/2} A D^{1/2} C \nu^{1/2}$, where I_p represents peak current, n , A , C , D and ν are number of electrons in reaction, electrode area, Li^+ concentration in electrolyte, and diffusion coefficient of Li^+ , and scan rate respectively. Considering n , A , C are constants, a reasonable estimate of Li^+ diffusion rate could be provided by computing the slope of linear fits for I_p versus $\nu^{1/2}$ [53]. Figures 3(c)–3(e) show the values of slope (as listed in Table S3 in the ESM) for anodic peak (Peak A1) and both cathodic peaks (Peak C1, Peak C2) of Ti-HEO/S/KB are higher than those of S/KB, indicating that Ti-HEO/S/KB has higher lithium-ion diffusion rate coupled with faster LPS-conversion kinetics. The results are well consistent with those obtained by using Li_2S_6

symmetric cells in which Ti-HEO is also demonstrated to have faster LPS-conversion kinetics. It is worth mentioning that affluent active sites resulting from randomly distributed multicomponent cations in Ti-HEOs with increased conductivities enable their outstanding electrochemical performance (Fig. 3(f)).

Moreover, CV in coin cells (CR2025-type) is used to further identify the enhanced LPS-conversion kinetics at $0.1 \text{ mV}\cdot\text{s}^{-1}$ (1.7 – 2.8 V versus Li/Li^+). The sulfur mass loading (1.2 – $1.5 \text{ mg}\cdot\text{cm}^{-2}$) and electrolyte to sulfur (E/S) ratio ($15 \mu\text{L}\cdot\text{mg}^{-1}$) are controlled in these typical LSBs. Figure S7(a) in the ESM demonstrates two distinct cathodic peaks (R_1 , R_2) at around $\sim 2.3 \text{ V}$ vs. Li/Li^+ and $\sim 2.02 \text{ V}$ vs. Li/Li^+ for Ti-HEO/S/KB and S/KB cathodes (70 wt.% sulfur content), in accord with the reduction of S_8 to soluble long-chain Li_2S_x ($4 \leq x \leq 8$) and further conversion to insoluble lithium Li_2S_x ($x=1,2$), respectively [54]. Two anodic peaks (O_1 , O_2) around $\sim 2.31 \text{ V}$ vs. Li/Li^+ and $\sim 2.37 \text{ V}$ vs. Li/Li^+ result from sulfide oxidation to polysulfide species and then to elemental sulfur. The catalytic performance of Ti-HEO on conversion kinetics could be further quantified using the Tafel slopes determined from the CV curves. In contrast to S/KB (34, 119, 76 $\text{mV}\cdot\text{dec}^{-1}$), Ti-HEO/S/KB cathode presents relatively smaller Tafel slopes of 23 and 22 $\text{mV}\cdot\text{dec}^{-1}$, respectively (Figs. S7(b)–S7(d) in the ESM), signifying the accelerated kinetics. The overlapping CV curves of consecutive redox cycles also indicate superior electrochemical reversibility (Fig. S8(a) in the ESM). Notably, the Ti-HEO/S/KB cathodes exhibit a larger peak current and a significant positive shift in reduction potentials (~ 2.31 and $\sim 2.02 \text{ V}$ vs. Li/Li^+) as compared to S/KB (~ 2.27 and $\sim 2.0 \text{ V}$ vs. Li/Li^+) (Fig. S8(b) in the ESM). Meanwhile, oxidation peaks are considerably shifted towards a lower potential (Fig. S8(c) in the ESM), implying the enhanced bidirectional LPS-conversion kinetics, catalytic effect and superior sulfur utilization. These

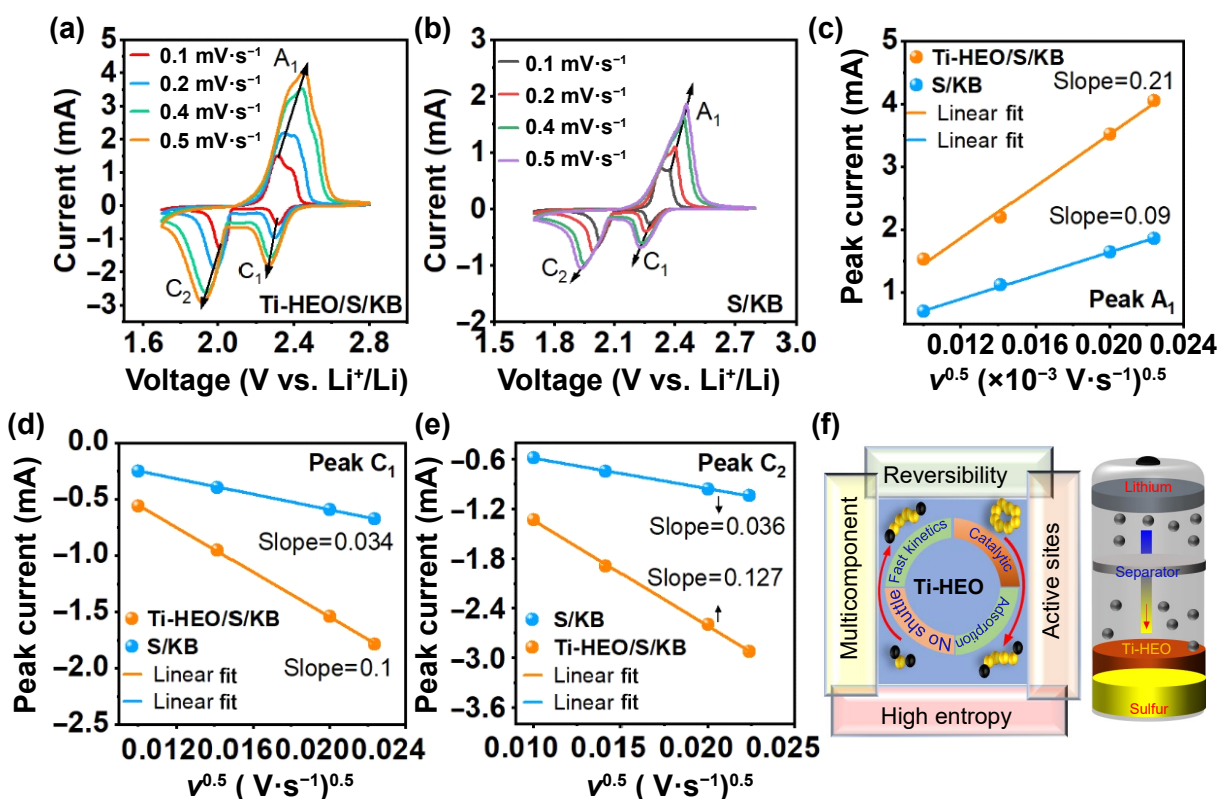


Figure 3 (a) CV curves of Ti-HEO/S/KB cathodes and (b) S/KB cells at different scan rates. (c) Linear fitting of peak current and scan rate square root of anodic oxidation (peak A₁). Linear fitting of peak current and scan rate square root for (d) the 1st cathodic reduction (peak C₁) and (e) the 2nd cathodic reduction (peak C₂). (f) Schematic diagram illustrating the Ti-HEO catalytic characteristics in Li-S batteries.

results clearly indicate that the Ti-HEO with improved electrical conductivity could be prepared by the calcination of M-MOFs at low temperature as developed in this work, which could effectively lower the overpotential, facilitate LPS-conversion kinetics, and improve the life span of LSBs.

3.3 Electrochemical performances

Figure 4(a) depicts the magnified plateaus observed in the galvanostatic charge/discharge (GCD) profile at the rate of 0.1 C for both the first and 100th cycles of Ti-HEO/S/KB, in comparison to the GCD profile of S/KB cathodes. These results indicate enhanced redox kinetics and superior utilization of sulfur in the Ti-HEO/S/KB system [46, 55]. Elemental sulfur (S₈) converting to long-chain soluble Li₂S_x (4 ≤ x ≤ 8) may be responsible for the initial discharge plateau at the high voltage platform (~2.3 V vs. Li/Li⁺). The 2nd plateau at the low voltage platform (~2.1 V vs. Li/Li⁺) corresponds to subsequent conversion of soluble LPS to the insoluble final product (Li₂S₂/Li₂S). Besides, a continuous charge plateau (~2.3 V vs. Li/Li⁺) could be ascribed to reverse reactions [56]. The efficient anchoring of the soluble LPS in the high voltage region (2.8–2.3 V vs. Li/Li⁺) could provide the battery with a higher discharge capacity. The Ti-HEO/S/KB cathode delivers a higher initial discharge capacity at 0.1 C (~1375 mAh·g⁻¹) compared to S/KB cathode (~1025 mAh·g⁻¹). Notably, Ti-HEO/S/KB cathode has a superior anchoring of LPS as evidenced by a higher ratio of the capacities of the two plateaus (i.e., Q_L/Q_H, 2.09) compared to S/KB (1.93) (Fig. 4(b)). Additionally, the voltage hysteresis (ΔE) between charge and discharge plots for Ti-HEO/S/KB cathode (~184 mV) is less than that of HEO850/S/KB (~200 mV) (our previously reported work) [42], and S/KB (~246 mV), indicating the further decreased polarization (Fig. 4(b)). It

could be because of the increased electrical conductivity of Ti-HEO, resulting in an improved battery rate performance. Figure 4(c) demonstrates that the polarization potential gap increases with increasing current rate. It is worth mentioning that the shape of charge/discharge plateaus is kept even at higher current rates, implying that the Ti-HEO facilitates efficient Li⁺ ion transportation. The quick-charging capability of Ti-HEO/S/KB, HEO850/S/KB (our previously reported work) [42] and S/KB cathodes having ~1.2 mg·cm⁻² sulfur loading is evaluated at current rates varied from 0.1 to 1 C, sustained for 5 cycles at each step and abruptly returned to 0.1 C. The Ti-HEO/S/KB cathode shows high initial discharge capacities of ~1590, 1397, 1238, 1101 mAh·g⁻¹ at 0.1, 0.2, 0.5, and 1 C, which are significantly better than those of reported HEO850/S/KB [42] (~1513, 1330, 1147, and 985 mAh·g⁻¹), and S/KB (~646, 432, 326, and 266 mAh·g⁻¹) at the corresponding current rates. Returning the current to 0.1 C allows Ti-HEO/S/KB to reach a capacity of ~1298 mAh·g⁻¹, again exceeding that of reported HEO850/S/KB (~1236 mAh·g⁻¹) [42] and S/KB (~463 mAh·g⁻¹) as shown in the Fig. 4(d). The enhanced rate performance can stem from the higher electrical conductivity exhibited by titanium-containing high entropy oxides (Ti-HEOs), which possess effective electrocatalytic characteristics over LPS conversion.

The enhancement of battery energy density is commonly acknowledged to be associated with a lower electrolyte-to-sulfur (E/S) ratio [57, 58]. Nevertheless, the electrochemical performance of batteries containing LPS is consistently challenging because of the occurrence of solid-liquid-solid phase transitions during the charging and discharging cycle. Various Ti-HEO/S/KB cathode typical batteries with a high sulfur loading (~4 mg·cm⁻²) are assembled with different E/S ratios (i.e., 10 and 6 μL·mg⁻¹). The

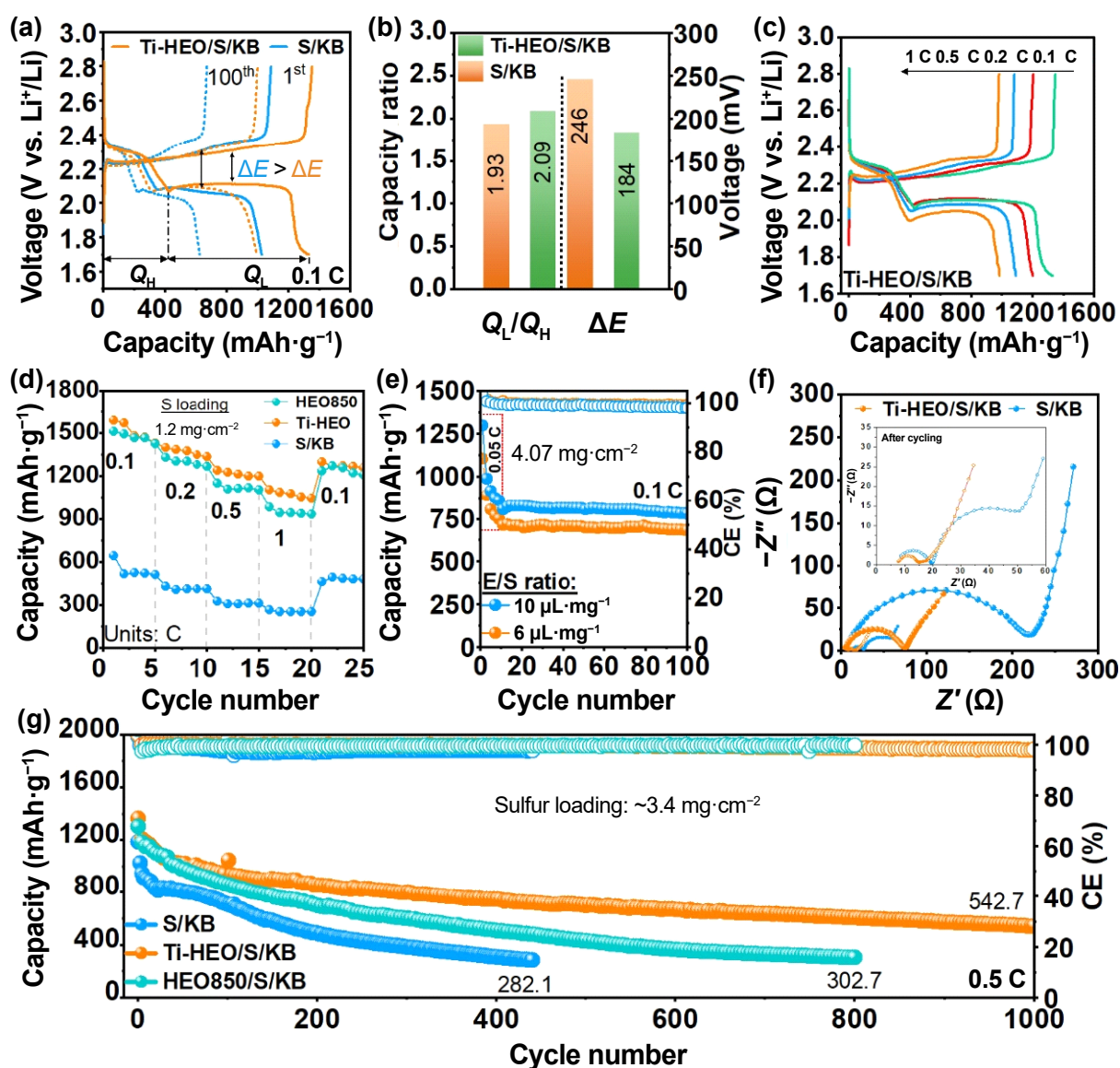


Figure 4 (a) GCD profiles of the 1st and 100th cycles are compared for the Ti-HEO/S/KB and S/KB cathode. (b) First plateau specific discharge capacity (Q_H) to second plateaus specific discharge capacity (Q_L) ratio and polarization potential gap of Ti-HEO/S/KB and S/KB half cells. (c) GCD plots at various current rates (i.e., 0.1, 0.2, 0.5, and 1 C). (d) Comparison of rate performance for the Ti-HEO/S/KB and S/KB cathodes. (e) Cycling performance of Ti-HEO/S/KB and S/KB cathodes with different E/S ratios. (f) Comparison of EIS for fresh and cycled electrodes (after 100 cycles). (g) Comparison of long-term cycling stability for Ti-HEO/S/KB, HEO850/S/KB, and S/KB under 0.5 C.

cells have an initial discharge capacity of $\sim 881 \text{ mAh}\cdot\text{g}^{-1}$ with an E/S ratio of $10 \mu\text{L}\cdot\text{mg}^{-1}$ at 0.1 C (activation for 5 cycles at 0.05 C), and discharge capacity could be retained at 86% of initial one after 100 cycles. With E/S ratio further decreased to $6 \mu\text{L}\cdot\text{mg}^{-1}$, the Ti-HEO/S/KB cathode containing typical batteries still endows a high discharge capacity of $\sim 780 \text{ mAh}\cdot\text{g}^{-1}$, which is retained at $\sim 682 \text{ mAh}\cdot\text{g}^{-1}$ after 100 cycles at 0.1 C (Fig. 4(e)). Moreover, the optical images (Fig. S9 in the ESM) of the lithium foil after undergoing 100 cycles demonstrate a discernible distinction when utilizing the Ti-HEO/S/KB cathode as opposed to the regular S/KB cathode. These images may provide evidence of a decreased occurrence of parasitic reactions on the lithium anode. These findings clearly signify that Ti-HEO with elevated electrical conductivity promotes the rapid conversion of LPS even at low electrolyte to sulfur ratios leading to better cycling performance of LSBs.

Additional testing includes electrochemical impedance spectroscopy (EIS) on freshly manufactured typical Li-S cells

before cycling and again after 100th GCD cycle (at full charge state, 2.8 V vs. Li/Li⁺). The typical Nyquist plots containing an intersection in high-frequency region, a semicircle at high-to-medium frequency zone, and an upward line in low-frequency region, which efficiently characterize the electrolyte resistance (R_0), charge transfer resistance (R_{ct}), and diffusion resistance (R_d) of Li⁺ ions into the solid cathode, respectively. It is worth mentioning that the Ti-HEO/S/KB cathode offers a lower charge transfer resistance ($\sim 150 \Omega$) in comparison to the S/KB ($\sim 220 \Omega$) cathode, as indicated by smaller semicircle at high-medium frequency range of Nyquist plots for Ti-HEO/S/KB (Fig. 4(f)). A new semicircle has emerged in the EIS spectra after the 100th cycle, which might be referred to as solid electrolyte interface (SEI) resistance (R_s). Notably, the newly emerged semicircle for Ti-HEO/S/KB cathode is significantly smaller than that for S/KB cathode, indicating a greater redispersion of sulfur species on the surface of electrode, which may favor the extended cycle life of Li-

S batteries. The significant decrease in the impedance upon cycling may be attributed to activation of sulfur cathode, enhanced sulfur utilization, and stable and well-formed electrode/electrolyte interface. This interface is crucial for efficient charge transfer and ion transport between the cathode and electrolyte. With cycling, the interface can become more stable, allowing for reduced interfacial resistance and improved electrochemical kinetics, leading to lower impedance (Inset: Fig. 4(f)).

Figure 4(g) shows cycling stability (0.5 C) comparison of Ti-HEO/S/KB cathode, our previously reported HEO850/S/KB [42], and S/KB. The Ti-HEO/S/KB cathode at a high areal sulfur mass loading of $\sim 3.4 \text{ mg}\cdot\text{cm}^{-2}$ shows a superior cycling stability after 1000 cycles. Ti-HEO/S/KB cells delivered a high initial discharge capacity of $\sim 1246 \text{ mAh}\cdot\text{g}^{-1}$, and it is retained at $\sim 542 \text{ mAh}\cdot\text{g}^{-1}$ with a low-capacity decay rate of 0.056% per cycle. In contrast, the reported HEO850/S/KB [42] electrode at the same areal sulfur mass loading ($\sim 3.4 \text{ mg}\cdot\text{cm}^{-2}$) exhibits a comparatively lower discharge capacity of $\sim 1178 \text{ mAh}\cdot\text{g}^{-1}$ in the first GCD cycle, which further decreased to $\sim 302 \text{ mAh}\cdot\text{g}^{-1}$ after 800 discharge/charge cycles at a moderate capacity fading rate of 0.093% per cycle. The S/KB cathode could only realize a lower initial discharge capacity of $\sim 1024 \text{ mAh}\cdot\text{g}^{-1}$ and because of the possible shuttling effect and sluggish conversion reaction of LPS, it is unable to keep the stable cycling performance and its capacity declines very fast to $\sim 282 \text{ mAh}\cdot\text{g}^{-1}$ only after 440 cycles, indicating a severe capacity decay rate of 0.164% per cycle. Again, the remarkable long-term cycling stability of Ti-HEO/S/KB batteries are due to improved electrical conductivity and accelerated catalytic conversion of LPS.

In addition, the electrochemical performances of the Ti-HEO/S/KB cathode are also compared to those of cathode containing similar Ti-based materials (Table S4 in the ESM). For example, Qi and co-workers reported effective utilization of MIL-125(Ti) derived carbon embedded with TiO_2 nanoparticles serving as sulfur host. The generated $\text{TiO}_2/\text{C}@S$ cathode with a areal sulfur mass loading of $\sim 2.0 \text{ mg}\cdot\text{cm}^{-2}$ delivered an initial discharge capacity of $\sim 1281 \text{ mAh}\cdot\text{g}^{-1}$ with a capacity decay rate of 0.39% per cycle over 100 cycles [59]. Microspheres of Magnéli phase Ti_4O_7 with improved electrical conductivity were produced by Liu and co-workers. The fabricated $\text{Ti}_4\text{O}_7@S$ composite cathode with a areal sulfur loading of $\sim 1.3 \text{ mg}\cdot\text{cm}^{-2}$ displayed an first discharge capacity of $\sim 1490 \text{ mAh}\cdot\text{g}^{-1}$ and stable cycling life over 500 cycles with a lower capacity fading rate of 0.09% per cycle [60]. Using anodization and subsequent reduction at high temperatures (850°C) in a hydrogen atmosphere, Wu and co-workers were able to report the synthesis of Magnéli phase Ti_4O_7 nanotube arrays (NTA) on the titanium nitride (TiN) mesh. The sulfur containing composite cathode (AB-S- Ti_4O_7 -NTA/S) fabricated by electrodeposition technique achieved an initial discharge capacity of $\sim 766 \text{ mAh}\cdot\text{g}^{-1}$ at 0.5 C, and the discharge capacity dropped to $\sim 357 \text{ mAh}\cdot\text{g}^{-1}$ after 1500 cycles with a sulfur loading of $\sim 1.3 \text{ mg}\cdot\text{cm}^{-2}$ [61]. Compared to those cathodes mentioned above, the Ti-HEO/S/KB composite cathode reported in this study exhibits higher initial discharge capacity ($\sim 1246 \text{ mAh}\cdot\text{g}^{-1}$ at 0.5 C) with lower capacity decay rate of 0.056% per cycle at a comparatively higher sulfur loading of $\sim 3.4 \text{ mg}\cdot\text{cm}^{-2}$. Therefore, it is believed that the enhanced electrical conductivity and electrocatalytic capabilities of single-phase Ti-HEO may account for the enhanced electrochemical performances of Li-S batteries with Ti-HEO/S/KB cathodes with high sulfur loadings.

In addition to cycling performance, the rate capability at high sulfur loadings represents another critical prerequisite for the practical application of Li-S batteries [57,62]. The rate

performance of typical Ti-HEO/S/KB cathode with $\sim 3.4 \text{ mg}\cdot\text{cm}^{-2}$ sulfur loading is systematically assessed by progressively increasing the current densities from 0.1 to 1 C. It delivers initial discharge capacities of ~ 1379 , 1255 , 1088 , and $985 \text{ mAh}\cdot\text{g}^{-1}$ at 0.1, 0.2, 0.5, and 1 C, respectively (Fig. S10(a) in the ESM). When the current rate is gradually recovered to 0.1 C, the reversible discharge capacities of ~ 1037 , 1100 , and $1155 \text{ mAh}\cdot\text{g}^{-1}$ at 0.5, 0.2, and 0.1 C, respectively, are obtained. Since the initial discharge capacities of reported HEO850/S/KB [42] are $\sim 1010 \text{ mAh}\cdot\text{g}^{-1}$ (0.1 C), $\sim 693 \text{ mAh}\cdot\text{g}^{-1}$ (0.2 C), $617 \text{ mAh}\cdot\text{g}^{-1}$ (0.5 C), and $505 \text{ mAh}\cdot\text{g}^{-1}$ (1 C), the Ti-HEO/S/KB cathode endows a higher specific capacity ($\sim 1155 \text{ mAh}\cdot\text{g}^{-1}$) than HEO850/S/KB ($\sim 620 \text{ mAh}\cdot\text{g}^{-1}$) when the current rate is returned to 0.1 C. The rate performance measurements on Ti-HEO/S/KB cells (S loading $\sim 3.2 \text{ mg}\cdot\text{cm}^{-2}$) at increasing C rates from 0.5 C to 4 C, sustained for 5 galvanostatic cycles at each step. The Ti-HEO/S/KB cathode exhibited acceptable discharge capacities: $\sim 1089 \text{ mAh}\cdot\text{g}^{-1}$ (0.5 C), $\sim 941 \text{ mAh}\cdot\text{g}^{-1}$ (1 C), $\sim 689 \text{ mAh}\cdot\text{g}^{-1}$ (2 C), and $\sim 373 \text{ mAh}\cdot\text{g}^{-1}$ (4 C), with a reversible capacity of $\sim 1009 \text{ mAh}\cdot\text{g}^{-1}$ upon returning to 0.5 C (Fig. S10(b) in the ESM). Ti-HEO/S/KB cathode, with an elevated sulfur loading of $3.2\text{--}3.4 \text{ mg}\cdot\text{cm}^{-2}$, has significantly better rate performance, that should be because of its enhanced electrical conductivity. Moreover, the Ti-HEO/S/KB cathodes with a further increased sulfur loading (~ 4.3 or $5.0 \text{ mg}\cdot\text{cm}^{-2}$) are also prepared with same slurry coating method on carbon cloth, and their cycling performance is tested at 0.2 C with a typical E/S ratio of $15 \mu\text{L}\cdot\text{mg}^{-1}$. After the cells are activated at low current densities (i.e., 0.05 C and 0.1 C) for 10 cycles each, those cathodes deliver a discharge capacity of $\sim 850 \text{ mAh}\cdot\text{g}^{-1}$ on the first cycle, which is maintained at $\sim 790 \text{ mAh}\cdot\text{g}^{-1}$ after 130 cycles. It is worth mentioning that the cell with a higher sulfur loading of $\sim 5.0 \text{ mg}\cdot\text{cm}^{-2}$ also exhibits a high initial discharge capacity of $\sim 607 \text{ mAh}\cdot\text{g}^{-1}$, and the discharge capacity can be still maintained at $\sim 500 \text{ mAh}\cdot\text{g}^{-1}$ after 130 cycles with an acceptable average Coulombic efficiency (CE) of 98.5% (Fig. S10(c) in the ESM). The findings affirm that Ti-HEO serves as an effective anchor for LPS, facilitating accelerated LPS conversion kinetics. This is attributed to the enhanced electrical conductivity and electro-catalytic properties of Ti-HEO. Consequently, Li-S batteries exhibit prolonged cycling stability, even when subjected to high sulfur loadings.

3.4 Self-discharge measurement

The capability of Li-S batteries to withstand self-discharge for an adequate amount of time is regarded as an additional key criteria for their commercial viability [63]. Using a three-step test protocol, self-discharging in Ti-HEO/S/KB cells is systematically investigated [64]. Measurements for self-discharge evaluation include regular discharge capacity (RC) while cycling, delivered capacity at varied set value of voltage (C_T), and remaining discharge capacity (C_R), as shown in Figs. 5(a) and 5(b). The cells are allowed to discharge up to a predetermined specific voltage level and held at rest for 48 hours to observe the self-discharging (SD), as shown in Fig. 5(c). The specific capacity and open circuit voltage are both monitored. Ti-HEO/S/KB electrode with a high sulfur loading of $\sim 3.7 \text{ mg}\cdot\text{cm}^{-2}$ exhibits a discharge capacity of $\sim 1105 \text{ mAh}\cdot\text{g}^{-1}$ for the first cycle at 0.1 C, and the discharge capacity is maintained at $\sim 925 \text{ mAh}\cdot\text{g}^{-1}$ (83% capacity retention) after resting at each depth of discharge for 48 hours, as shown in Fig. 5(d), implying the effective LPS anchoring. Another SD test with a resting duration of 480 hours (20 days) is also conducted for comparisons. The fully charged cells (2.8 V) with the Ti-

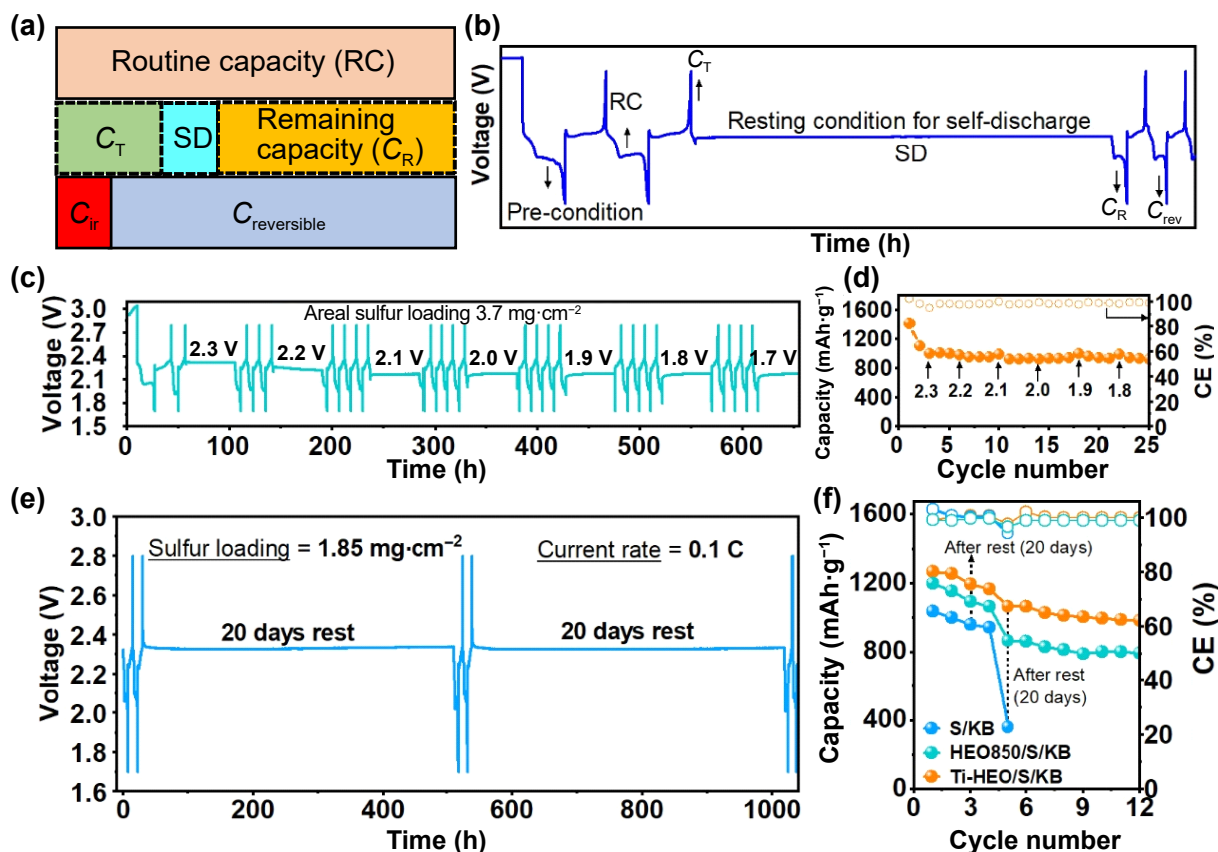


Figure 5 (a) Schematic diagram depicting various types of capacities considered in evaluating the self-discharging. (b) The testing procedure developed to investigate self-discharging. (c) Open circuit voltage (OCV) profiles during resting of 48 hours at specific depths of discharge. (d) Specific discharge capacities delivered after resting for self-discharge measurement. (e) OCV monitored during resting for 20 days of Ti-HEO/S/KB batteries. (f) Comparison of specific discharge capacity after resting of 20 days.

HEO/S/KB, reported HEO850/S/KB [42], and S/KB cathodes (with a sulfur loading of $\sim 1.8 \text{ mg}\cdot\text{cm}^{-2}$) are subjected to rest during the 3rd and 5th discharge cycles (Fig. 5(e)). Notably, the Ti-HEO/S/KB cathode displays a lower self-discharging capacity loss as compared to those of other cathodes (i.e., HEO850/S/KB and S/KB). It shows a greater initial discharge capacity of $\sim 1256 \text{ mAh}\cdot\text{g}^{-1}$, and it is maintained at $\sim 1064 \text{ mAh}\cdot\text{g}^{-1}$ ($\sim 84\%$ capacity retention) after resting for 20 days during the 3rd and 5th discharge cycles. Since the reported HEO850/S/KB [42] cathode demonstrates 72% capacity retention after resting and it has an initial discharge capacity of $\sim 1201 \text{ mAh}\cdot\text{g}^{-1}$, the S/KB cathode shows significantly low initial discharge specific capacity ($\sim 1037 \text{ mAh}\cdot\text{g}^{-1}$) in the first cycle and experiences sudden failure after resting (Fig. 5(f)). The failure of S/KB cells could be associated with the sluggish conversion and severe shuttling of LPS. Compared to other cathodes studied, the Ti-HEO/S/KB cathode demonstrates a better anti-self-discharging ability by maintaining the battery voltage at $\sim 2.352 \text{ V}$ for a prolonged period (i.e., 20 days resting).

3.5 Ex-situ TEM analysis of cycled electrodes

The microstructure characteristics of both cycled and freshly prepared electrodes are obtained by *ex-situ* TEM analysis. Figure S11(a) in the ESM depicts the Ti-HEO particles with irregular shapes in the Ti-HEO/S/KB composite, and the HRTEM image (Fig. S11(b) in the ESM) reveals their crystalline characteristics as reflected by the clear lattice fringes, which indicate a d-spacing of 0.24 nm corresponding to (111) plane of the rocksalt structure in

consistent with that determined from XRD results. It is worth mentioning that after 375 redox cycles under sulfur loading of $2.3 \text{ mg}\cdot\text{cm}^{-2}$, the Ti-HEO/S/KB cathode (fully charged at $\sim 2.8 \text{ V}$) still maintains its original irregular morphology (Fig. S11(c) in the ESM). However, various dense and dark patches are witnessed on the surface that could be because of the deposition of Li_2S or sulfur aggregates on the surface of electrode. The HRTEM image (Fig. S11(d) in the ESM) further confirms the formation of crystalline Li_2S in the electrode architecture. The results indicate that the enhanced cycling performance, faster redox kinetics and efficient polysulfide adsorption of Ti-HEO/S/KB are reliant on the randomly distributed metal ions, its structural stability during redox cycling and enhanced electrical conductivity of the Ti-HEO.

4 Conclusion

In summary, Ti-HEO or $(\text{Ni}_{0.2}\text{Co}_{0.2}\text{Fe}_{0.2}\text{Mg}_{0.2}\text{Ti}_{0.2})\text{O}$ with enhanced electrical conductivities is successfully fabricated through calcining MOF templates at modest temperature (850°C). The as-synthesized Ti-HEO particles exhibit irregular shapes with an average size of $\sim 562 \text{ nm}$, excellent phase stability and phase reversibility. Since the Ti-HEO electrodes have abundant exposed active sites with numerous cations, they work well as sulfur cathodes in LSBs, accelerating the LPS-conversion kinetics and successfully suppressing the shuttling effect. The Ti-HEO/S/KB cathodes (with a sulfur loading of $\sim 3.4 \text{ mg}\cdot\text{cm}^{-2}$) achieve a high initial discharge capacity of $\sim 1246 \text{ mAh}\cdot\text{g}^{-1}$ at 0.5 C , and the discharge capacity is maintained at $\sim 542 \text{ mAh}\cdot\text{g}^{-1}$ with a capacity decay rate of 0.056% per cycle over 1000 cycles. The

voltage hysteresis of Ti-HEO/S/KB cathode (~184 mV) is also less than that of HEO850/S/KB (~200 mV), resulting in better rate performance of Ti-HEO/S/KB at an elevated sulfur loading. The Ti-HEO/S/KB cathode (with a sulfur loading of ~1.8 mg·cm⁻²) also showcases a significant suppression in the self-discharging capacity loss. It retains 84% of its initial capacity (~1256 mAh·g⁻¹ at 0.1 C) after prolonged resting for 20 days during the 3rd and 5th GCD cycles, respectively. The Ti-HEO/S/KB cathodes offer superior rate capability and long-term cycling performance to those of HEO850/S/KB cathodes even at the elevated sulfur loading. The remarkable electrochemical performance of Ti-HEO/S/KB cathodes could be ascribed to the increased electrical conductivity and catalytic properties provided by the entropy stabilized phase of Ti-HEO.

Acknowledgements

The authors are grateful for the following financial supports: the National Natural Science Foundation of China (Nos. 52372289 and 52102368), Guangdong Science and Technology Bureau (Grant Nos. 2019B090908001 and 2020A0505090011), Guangdong Special Fund for Key Areas (20237DZX3042), Shenzhen STI (Grant No. SGDXX20190816230615451), Shenzhen Stable Support Project, Guangdong-Hong Kong-Macao Joint Laboratory for Photonic-Thermal-Electrical Energy Materials and Devices (Grant No. 2019B121205001), Otto Poon Charitable Foundation (Grant Nos. 847W, CDBC, CDBW), and HKPolyU Postdoctoral Fellowships (Grant No. W28H).

Electronic Supplementary Material: Supplementary material (materials, syntheses of Ti-HEOs structures, Ti-HEO/S/KB, S/KB composite formation, cathode preparation and cell assembly, electrochemical testing conditions of LSBs, symmetric cell fabrication, self-discharge testing protocol, materials characterizations (SEM, EDX, XPS), CV comparison, Tafel slope, cycling and rate performance at elevated sulfur loading, TEM analysis of fresh and cycled electrodes, comparison of Ti-HEO with several medium entropy oxides, elemental content of Ti-HEO obtained from XPS results, $I_p/v^{0.5}$ slope values and comparison of our work with published reports) is available in the online version of this article at <https://doi.org/10.26599/NRE.2024.9120116>.

Declaration of conflicting interests

The authors declare that they have no known competing financial interests or personal relationships that could have appeared to influence the work reported in this paper.

Data availability

All data needed to support the conclusions in the paper are presented in the manuscript and/or the Supplementary Materials. Additional data related to this paper may be requested from the corresponding author upon request.

References

- [1] Zhou, G. M.; Chen, H.; Cui, Y. Formulating energy density for designing practical lithium-sulfur batteries. *Nat. Energy* **2022**, *7*, 312–319.
- [2] Xiang, Y. Y.; Lu, L. Q.; Kottapalli, A. G. P.; Pei, Y. T. Status and perspectives of hierarchical porous carbon materials in terms of high-performance lithium-sulfur batteries. *Carbon Energy* **2022**, *4*,

- 346–398.
- [3] Manthiram, A.; Fu, Y. Z.; Chung, S. H.; Zu, C. X.; Su, Y. S. Rechargeable lithium-sulfur batteries. *Chem. Rev.* **2014**, *114*, 11751–11787.
- [4] Seh, Z. W.; Sun, Y. M.; Zhang, Q. F.; Cui, Y. Designing high-energy lithium-sulfur batteries. *Chem. Soc. Rev.* **2016**, *45*, 5605–5634.
- [5] Fang, R. P.; Zhao, S. Y.; Sun, Z. H.; Wang, D. W.; Cheng, H. M.; Li, F. More reliable lithium-sulfur batteries: Status, solutions and prospects. *Adv. Mater.* **2017**, *29*, 1606823.
- [6] Bruce, P. G.; Freunberger, S. A.; Hardwick, L. J.; Tarascon, J. M. Li-O₂ and Li-S batteries with high energy storage. *Nat. Mater.* **2012**, *11*, 19–29.
- [7] Larcher, D.; Tarascon, J. M. Towards greener and more sustainable batteries for electrical energy storage. *Nat. Chem.* **2015**, *7*, 19–29.
- [8] Boyjoo, Y.; Shi, H. D.; Tian, Q.; Liu, S. M.; Liang, J.; Wu, Z. S.; Jaroniec, M.; Liu, J. Engineering nanoreactors for metal-chalcogen batteries. *Energy Environ. Sci.* **2021**, *14*, 540–575.
- [9] Zhang, J.; Li, M. N.; Younus, H. A.; Wang, B. S.; Weng, Q. H.; Zhang, Y.; Zhang, S. G. An overview of the characteristics of advanced binders for high-performance Li-S batteries. *Nano Mater. Sci.* **2021**, *3*, 124–139.
- [10] Ji, X. L.; Nazar, L. F. Advances in Li-S batteries. *J. Mater. Chem.* **2010**, *20*, 9821–9826.
- [11] Hagen, M.; Hanselmann, D.; Ahlbrecht, K.; Maça, R.; Gerber, D.; Tübke, J. Lithium-sulfur cells: The gap between the state-of-the-art and the requirements for high energy battery cells. *Adv. Energy Mater.* **2015**, *5*, 1401986.
- [12] Majumder, S.; Shao, M. H.; Deng, Y. F.; Chen, G. H. Ultrathin sheets of MoS₂/g-C₃N₄ composite as a good hosting material of sulfur for lithium-sulfur batteries. *J. Power Sources* **2019**, *431*, 93–104.
- [13] Majumder, S.; Shao, M. H.; Deng, Y. F.; Chen, G. H. Two dimensional WS₂/C nanosheets as a polysulfides immobilizer for high performance lithium-sulfur batteries. *J. Electrochem. Soc.* **2019**, *166*, A5386–A5395.
- [14] Liang, X.; Hart, C.; Pang, Q.; Garsuch, A.; Weiss, T.; Nazar, L. F. A highly efficient polysulfide mediator for lithium-sulfur batteries. *Nat. Commun.* **2015**, *6*, 5682.
- [15] Wang, H. Q.; Zhang, W. C.; Xu, J. Z.; Guo, Z. P. Advances in polar materials for lithium-sulfur batteries. *Adv. Funct. Mater.* **2018**, *28*, 1707520.
- [16] Zhang, Z. W.; Peng, H. J.; Zhao, M.; Huang, J. Q. Heterogeneous/homogeneous mediators for high-energy-density lithium-sulfur batteries: Progress and prospects. *Adv. Funct. Mater.* **2018**, *28*, 1707536.
- [17] Ji, X. L.; Lee, K. T.; Nazar, L. F. A highly ordered nanostructured carbon-sulphur cathode for lithium-sulphur batteries. *Nat. Mater.* **2009**, *8*, 500–506.
- [18] Xiao, Q. H. Q.; Yang, J. L.; Wang, X. D.; Deng, Y. R.; Han, P.; Yuan, N.; Zhang, L.; Feng, M.; Wang, C. A.; Liu, R. P. Carbon-based flexible self-supporting cathode for lithium-sulfur batteries: Progress and perspective. *Carbon Energy* **2021**, *3*, 271–302.
- [19] Raza, H.; Bai, S. Y.; Cheng, J. Y.; Majumder, S.; Zhu, H.; Liu, Q.; Zheng, G. P.; Li, X. F.; Chen, G. H. Li-S batteries: Challenges, achievements and opportunities. *Electrochem. Energy Rev.* **2023**, *6*, 29.
- [20] Shi, H. D.; Zhao, X. J.; Wu, Z. S.; Dong, Y. F.; Lu, P. F.; Chen, J.; Ren, W. C.; Cheng, H. M.; Bao, X. H. Free-standing integrated cathode derived from 3D graphene/carbon nanotube aerogels serving as binder-free sulfur host and interlayer for ultrahigh volumetric-energy-density lithium-sulfur batteries. *Nano Energy* **2019**, *60*, 743–751.
- [21] Dong, Y. F.; Zheng, S. H.; Qin, J. Q.; Zhao, X. J.; Shi, H. D.; Wang, X. H.; Chen, J.; Wu, Z. S. All-MXene-based integrated electrode constructed by Ti₃C₂ nanoribbon framework host and nanosheet interlayer for high-energy-density Li-S batteries. *ACS Nano* **2018**, *12*, 2381–2388.
- [22] Shi, H. D.; Qin, J. Q.; Huang, K.; Lu, P. F.; Zhang, C. F.; Dong, Y.

- F.; Ye, M.; Liu, Z. M.; Wu, Z. S. A two-dimensional mesoporous polypyrrole-graphene oxide heterostructure as a dual-functional ion redistributor for dendrite-free lithium metal anodes. *Angew. Chem.* **2020**, *132*, 12245–12251.
- [23] Ci, H. N.; Shi, Z. X.; Wang, M. L.; He, Y.; Sun, J. Y. A review in rational design of graphene toward advanced Li-S batteries. *Nano Res. Energy* **2023**, *2*, e9120054.
- [24] Sun, D. D.; Sun, Z. P.; Yang, D. H.; Jiang, X. F.; Tang, J.; Wang, X. B. Advances in boron nitride-based materials for electrochemical energy storage and conversion. *EcoEnergy* **2023**, *1*, 375–404.
- [25] Shi, H. D.; Ren, X. M.; Lu, J. M.; Dong, C.; Liu, J.; Yang, Q. H.; Chen, J.; Wu, Z. S. Dual-functional atomic zinc decorated hollow carbon nanoreactors for kinetically accelerated polysulfides conversion and dendrite free lithium sulfur batteries. *Adv. Energy Mater.* **2020**, *10*, 2002271.
- [26] He, J. R.; Manthiram, A. A review on the status and challenges of electrocatalysts in lithium-sulfur batteries. *Energy Storage Mater.* **2019**, *20*, 55–70.
- [27] Wang, Y. C.; Pu, Y. R.; Yuan, L.; Zhang, Y.; Liu, C.; Wang, Q.; Wu, H. Synergistic effect of WN/Mo₂C embedded in bioderived carbon nanofibers: A rational design of a shuttle inhibitor and an electrocatalyst for lithium-sulfur batteries. *ACS Appl. Mater. Interfaces* **2022**, *14*, 18578–18588.
- [28] Wang, S. N.; Hu, R. M.; Yuan, D.; Zhang, L.; Wu, C.; Ma, T. Y.; Yan, W.; Wang, R.; Liu, L.; Jiang, X. C. et al. Single-atomic tungsten-doped Co₃O₄ nanosheets for enhanced electrochemical kinetics in lithium-sulfur batteries. *Carbon Energy* **2023**, *5*, e329.
- [29] Wang, Z. F.; Yan, Y. J.; Zhang, Y. G.; Chen, Y. X.; Peng, X. Y.; Wang, X.; Zhao, W. M.; Qin, C. L.; Liu, Q.; Liu, X. J. et al. Single-atomic Co-B₂N₂ sites anchored on carbon nanotube arrays promote lithium polysulfide conversion in lithium-sulfur batteries. *Carbon Energy* **2023**, *5*, e306.
- [30] Shi, H. D.; Qin, J. Q.; Lu, P. F.; Dong, C.; He, J.; Chou, X. J.; Das, P.; Wang, J. M.; Zhang, L. Z.; Wu, Z. S. Interfacial engineering of bifunctional niobium (V)-based heterostructure nanosheet toward high efficiency lean-electrolyte lithium-sulfur full batteries. *Adv. Funct. Mater.* **2021**, *31*, 2102314.
- [31] Abraham, A. M.; Boteju, T.; Ponnurangam, S.; Thangadurai, V. A global design principle for polysulfide electrocatalysis in lithium-sulfur batteries-A computational perspective. *Battery Energy* **2022**, *1*, 20220003.
- [32] Rost, C. M.; Sachet, E.; Borman, T.; Moballegh, A.; Dickey, E. C.; Hou, D.; Jones, J. L.; Curtarolo, S.; Maria, J. P. Entropy-stabilized oxides. *Nat. Commun.* **2015**, *6*, 8485.
- [33] Murty, B. S.; Yeh, J. W.; Ranganathan, S. High-entropy alloys: Basic concepts. In *High Entropy Alloys*. Murty, B. S.; Yeh, J. W.; Ranganathan, S., Eds.; Elsevier: Amsterdam, 2014; pp 13–35.
- [34] Amiri, A.; Shahbazian-Yassar, R. Recent progress of high-entropy materials for energy storage and conversion. *J. Mater. Chem. A* **2021**, *9*, 782–823.
- [35] Wang, Q. S.; Sarkar, A.; Li, Z. Y.; Lu, Y.; Velasco, L.; Bhattacharya, S. S.; Brezesinski, T.; Hahn, H.; Breitung, B. High entropy oxides as anode material for Li-ion battery applications: A practical approach. *Electrochem. Commun.* **2019**, *100*, 121–125.
- [36] Ghigna, P.; Airolidi, L.; Fracchia, M.; Callegari, D.; Anselmi-Tamburini, U.; D'Angelo, P.; Pianta, N.; Ruffo, R.; Cibini, G.; de Souza, D. O. et al. Lithiation mechanism in high-entropy oxides as anode materials for Li-ion batteries: An *operando* XAS study. *ACS Appl. Mater. Interfaces* **2020**, *12*, 50344–50354.
- [37] Tian, L. Y.; Zhang, Z.; Liu, S.; Li, G. R.; Gao, X. P. High-entropy spinel oxide nanofibers as catalytic sulfur hosts promise the high gravimetric and volumetric capacities for lithium-sulfur batteries. *Energy Environ. Mater.* **2022**, *5*, 645–654.
- [38] Sarkar, A.; Velasco, L.; Wang, D.; Wang, Q. S.; Talasila, G.; de Biasi, L.; Kübel, C.; Brezesinski, T.; Bhattacharya, S. S.; Hahn, H. et al. High entropy oxides for reversible energy storage. *Nat. Commun.* **2018**, *9*, 3400.
- [39] Chen, Y. W.; Fu, H. Y.; Huang, Y. Y.; Huang, L. Q.; Zheng, X. Y.; Dai, Y. M.; Huang, Y. H.; Luo, W. Opportunities for high-entropy materials in rechargeable batteries. *ACS Mater. Lett.* **2021**, *3*, 160–170.
- [40] Tsau, C. H.; Yang, Y. C.; Lee, C. C.; Wu, L. Y.; Huang, H. J. The low electrical resistivity of the high-entropy alloy oxide thin films. *Procedia Eng.* **2012**, *36*, 246–252.
- [41] Yang, Y. C.; Tsau, C. H.; Yeh, J. W. TiFeCoNi oxide thin film-A new composition with extremely low electrical resistivity at room temperature. *Scr. Mater.* **2011**, *64*, 173–176.
- [42] Raza, H.; Cheng, J. Y.; Lin, C.; Majumder, S.; Zheng, G. P.; Chen, G. H. High-entropy stabilized oxides derived via a low-temperature template route for high-performance lithium-sulfur batteries. *EcoMat* **2023**, *5*, e12324.
- [43] Raza, H.; Cheng, J. Y.; Chen, G. H.; Zheng, G. P. Low-temperature calcination of metal-organic frameworks (MOFs) to derive the high entropy stabilized oxide for high performance lithium-sulfur batteries. *ECS Meet. Abstr.* **2022**, *IMA2022-0*, 2432.
- [44] Cheng, J. Y.; Ran, S. J.; Li, T.; Yan, M.; Wu, J.; Boles, S.; Liu, B.; Raza, H.; Ullah, S.; Zhang, W. J. et al. Achieving superior tensile performance in individual metal-organic framework crystals. *Adv. Mater.* **2023**, *35*, 2210829.
- [45] Zhao, Y. H.; Lai, X. Q.; Wang, P. F.; Liu, Z. L.; Yi, T. F. Construction of metal-organic framework-derived Al-doped Na₃V₂(PO₄)₃ cathode materials toward high-performance rechargeable Na-ion battery. *Energy Mater. Devices*, in press, DOI: 10.26599/EMD.2024.9370002.
- [46] Zheng, Y. N.; Yi, Y. K.; Fan, M. H.; Liu, H. Y.; Li, X.; Zhang, R.; Li, M. T.; Qiao, Z. A. A high-entropy metal oxide as chemical anchor of polysulfide for lithium-sulfur batteries. *Energy Storage Mater.* **2019**, *23*, 678–683.
- [47] Kheradmandfard, M.; Minouei, H.; Tsvetkov, N.; Vayghan, A. K.; Kashani-Bozorg, S. F.; Kim, G.; Hong, S. I.; Kim, D. E. Ultrafast green microwave-assisted synthesis of high-entropy oxide nanoparticles for Li-ion battery applications. *Mater. Chem. Phys.* **2021**, *262*, 124265.
- [48] Qiu, N.; Chen, H.; Yang, Z. M.; Sun, S.; Wang, Y.; Cui, Y. H. A high entropy oxide (Mg_{0.2}Co_{0.2}Ni_{0.2}Cu_{0.2}Zn_{0.2}O) with superior lithium storage performance. *J. Alloys Compd.* **2019**, *777*, 767–774.
- [49] Khan, N. A.; Akhavan, B.; Zheng, Z.; Liu, H. W.; Zhou, C. F.; Zhou, H. R.; Chang, L.; Wang, Y.; Liu, Y. P.; Sun, L. X. et al. Nanostructured AlCoCrCu_{0.5}FeNi high entropy oxide (HEO) thin films fabricated using reactive magnetron sputtering. *Appl. Surf. Sci.* **2021**, *553*, 149491.
- [50] Zhao, X. J.; Gao, T. Q.; Yuan, Y.; Fang, Z. Hollow slightly oxidized CoP confined into flyover-type carbon skeleton with multiple channels as an effective adsorption-catalysis matrix for robust Li-S batteries. *Electrochim. Acta* **2022**, *422*, 140512.
- [51] Lin, H. B.; Yang, L. Q.; Jiang, X.; Li, G. C.; Zhang, T. R.; Yao, Q. F.; Zheng, G. W.; Lee, J. Y. Electrocatalysis of polysulfide conversion by sulfur-deficient MoS₂ nanoflakes for lithium-sulfur batteries. *Energy Environ. Sci.* **2017**, *10*, 1476–1486.
- [52] Li, W. L.; Qian, J.; Zhao, T.; Ye, Y. S.; Xing, Y.; Huang, Y. X.; Wei, L.; Zhang, N. X.; Chen, N.; Li, L. et al. Boosting high-rate Li-S batteries by an MOF-derived catalytic electrode with a layer-by-layer structure. *Adv. Sci.* **2019**, *6*, 1802362.
- [53] Zhou, L.; Danilov, D. L.; Qiao, F.; Eichel, R. A.; Notten, P. H. L. ZnFe₂O₄ hollow rods enabling accelerated polysulfide conversion for advanced lithium-sulfur batteries. *Electrochim. Acta* **2022**, *414*, 140231.
- [54] Wang, S. X.; Liu, X. Y.; Duan, H. H.; Deng, Y. F.; Chen, G. H. Fe₃C/Fe nanoparticles embedded in N-doped porous carbon nanosheets and graphene: A thin functional interlayer for PP separator to boost performance of Li-S batteries. *Chem. Eng. J.* **2021**, *415*, 129001.
- [55] Mu, J. W.; Jiang, H. L.; Yu, M.; Gu, S. H.; He, G. H.; Dai, Y.; Li, X. C. Thiophilic-lithiophilic hierarchically porous membrane-enabled full lithium-sulfur battery with a low N/P ratio. *ACS Appl. Mater. Interfaces* **2022**, *14*, 23408–23419.

- [56] Abualela, S.; Lv, X. X.; Hu, Y.; Abd-Alla, M. D. NiO nanosheets grown on carbon cloth as mesoporous cathode for high-performance lithium-sulfur battery. *Mater. Lett.* **2020**, *268*, 127622.
- [57] Bhargav, A.; He, J. R.; Gupta, A.; Manthiram, A. Lithium-sulfur batteries: Attaining the critical metrics. *Joule* **2020**, *4*, 285–291.
- [58] Ye, H. L.; Li, Y. G. Towards practical lean-electrolyte Li-S batteries: Highly solvating electrolytes or sparingly solvating electrolytes. *Nano Res. Energy* **2022**, *1*, e9120012.
- [59] Qi, C.; Li, H. L.; Wang, J.; Zhao, C. C.; Fu, C. M.; Wang, L. N.; Liu, T. X. Metal-organic-framework-derived porous carbon embedded with TiO₂ nanoparticles as a cathode for advanced lithium-sulfur batteries. *ChemElectroChem* **2021**, *8*, 90–95.
- [60] Liu, M. T.; Jhulki, S.; Sun, Z. F.; Magasinski, A.; Hendrix, C.; Yushin, G. Atom-economic synthesis of Magnéli phase Ti₄O₇ microspheres for improved sulfur cathodes for Li-S batteries. *Nano Energy* **2021**, *79*, 105428.
- [61] Wu, H. W.; Hu, X. J.; Shao, M. H.; Zhang, S. W.; Chen, G. H. Encapsulating sulphur inside Magnéli phase Ti₄O₇ nanotube array for high performance lithium sulphur battery cathode. *Can. J. Chem. Eng.* **2022**, *100*, 2417–2431.
- [62] Liu, H. T.; Liu, F.; Qu, Z. H.; Chen, J. L.; Liu, H.; Tan, Y. Q.; Guo, J. B.; Yan, Y.; Zhao, S.; Zhao, X. S. et al. High sulfur loading and shuttle inhibition of advanced sulfur cathode enabled by graphene network skin and N, P, F-doped mesoporous carbon interfaces for ultra-stable lithium sulfur battery. *Nano Res. Energy* **2023**, *2*, e9120049.
- [63] Xiao, S. J.; Huang, L.; Lv, W.; He, Y. B. A highly efficient ion and electron conductive interlayer to achieve low self-discharge of lithium-sulfur batteries. *ACS Appl. Mater. Interfaces* **2022**, *14*, 1783–1790.
- [64] Knap, V.; Stroe, D. I.; Swierczynski, M.; Teodorescu, R.; Schaltz, E. Investigation of the self-discharge behavior of lithium-sulfur batteries. *J. Electrochem. Soc.* **2016**, *163*, A911–A916.



Hassan Raza received his B.E. degree from BZ University Multan, Pakistan in 2011 and master's degree from University of Engineering and Technology, Lahore, Pakistan in 2017. He obtained his Ph.D. from The Hong Kong Polytechnic University, Hong Kong, China. His current research interest focuses on the development and application of the high entropy stabilized oxides/sulfides (HEOs/HESs) in high-performance lithium-sulfur batteries.



Junye Cheng received his Ph.D. degree from City University of Hong Kong in 2019. Currently, he is an Associate Professor at Shenzhen MSU-BIT University. His current research interests focus on the development of low-dimensional nanomaterials for applications in energy storage and conversion, environmental protection, as well as electromagnetic wave absorption.



Guangping Zheng received his B.Sc. and M.Sc. degrees in Condensed Matter Physics from Sun Yat-sen University in 1991 and 1993. He obtained his Ph.D. in Materials Science and Engineering from Johns Hopkins University. He was a postdoctoral fellow at Georgia Institute of Technology from 2002 to 2004. Before Joining the Hong Kong Polytechnic University, he was a Research Assistant Professor at the University of Hong Kong. Prof. Zheng's research is in the areas of computational materials science, nano mechanics, electrocaloric effect, dielectric properties, and applications of nanomaterials in energy conversion and storage.



Guohua Chen obtained his B.Eng. degree from Dalian University of Technology in 1984, M.Eng. and Ph.D. degrees from McGill University, respectively, in 1989 and 1994. Now he is Chair Professor at City University of Hong Kong. Professor Chen's research is in the area of developing advanced materials for lithium/sodium ion batteries and Li-S batteries. He is a Fellow of HKIE, AIChE, Global Academy of Chinese Chemical Engineers. He is also elected as a Fellow of the Canadian Academy of Engineering.